



Automated bleeding detection in wireless capsule endoscopy images based on color feature extraction from Gaussian mixture model superpixels

S. Rathnamala¹ · S. Jenicka²

Received: 18 June 2020 / Accepted: 19 March 2021 / Published online: 10 April 2021
© International Federation for Medical and Biological Engineering 2021

Abstract

Wireless capsule endoscopy is the commonly employed modality in the treatment of gastrointestinal tract pathologies. However, the time taken for interpretation of these images is very high due to the large volume of images generated. Automated detection of disorders with these images can facilitate faster clinical interventions. In this paper, we propose an automated system based on Gaussian mixture model superpixels for bleeding detection and segmentation of candidate regions. The proposed system is realized with a classic binary support vector machine classifier trained with seven features including color and texture attributes extracted from the Gaussian mixture model superpixels of the WCE images. On detection of bleeding images, bleeding regions are segmented from them, by incrementally grouping the superpixels based on deltaE color differences. Tested with standard datasets, this system exhibits best performance compared to the state-of-the-art approaches with respect to classification accuracy, feature selection, computational time, and segmentation accuracy. The proposed system achieves 99.88% accuracy, 99.83% sensitivity, and 100% specificity signifying the effectiveness of the proposed system in bleeding detection with very few classification errors.

Keywords Bleeding detection · Wireless capsule endoscopy · Superpixel · Gaussian mixture model · Support vector machine

1 Introduction

Advancements in medical imaging techniques have considerably improved diagnostic procedures and detection accuracies in the timely intervention of several pathologies. Wireless capsule endoscopy (WCE) is an indispensable procedure in the diagnosis and treatment of gastrointestinal (GI) tract diseases. With the discovery of WCE by Iddan et al. [1] in 2000, it has become a widely accepted methodology for the visualization of the GI tract, thanks to its safety and clinical values. This modality is commonly used in the detection of polyps, ulcers, tumors, Crohn's disease, colitis, etc. Though it is a

potential tool for the clinical assessment of the entire GI tract, this procedure is time-consuming which involves patient preparation before the imaging process. According to a recent study by Robertson and Singh [2], 30 to 120 min in average are required for the generation of endoscopic reports in imaging the small bowel. Furthermore, based on the nature of capsules used in the procedure, several images are captured per second, resulting in large volumes of images for clinical interpretations. Physical examination of each of these image frames is unrealistic to make clinical decisions.

Stimulated with the advancements in medical imaging technologies and image processing algorithms, computer-aided systems for diagnosis, prognosis, and treatment management of several pathologies have been successfully deployed. Particularly, in the recent years, representative works on non-invasive cancer diagnosis have been proposed in [3–5]. These approaches leverage the potential of breast mammography, and mathematical approaches such as interval differential equations and interval analysis-based image segmentation.

Similarly, machine vision techniques and mathematical image processing approaches can be employed in the analysis of

✉ S. Rathnamala
rathnamalaphd123@gmail.com

¹ Department of Information Technology, Sethu Institute of Technology, Virudhunagar District, Kariapatti, Tamil Nadu 626115, India

² Department of CSE, Sethu Institute of Technology, Virudhunagar District, Kariapatti, Tamil Nadu 626115, India

endoscopic image frames for bleeding detection, significantly reducing the examination times and improving diagnostic accuracies. Recent works on endoscopic image processing are focused on enhancement of the frames for improved visualization of region of interest (RoI). A human visual system (HVS)-guided feature linking model (FML) presented in [6] is demonstrated to eliminate streaking, saturation, and color mix-up artifacts compared to classical image enhancement models.

Bleeding in the upper or lower GI tract is a critical abnormality, which may be a symptom of peptic ulcers, cirrhosis of the liver, cancer, hemorrhoids, etc. Bleeding detection in the WCE images and localization of the bleeding region is very challenging due to the heterogeneities on the bleeding surfaces. Investigations on computer-aided detection of GI bleeding have resulted in the formulation and solution of several pattern recognition and classification problems.

In the most recent work in this context proposed in [7], the RoI is realized as a set of key points obtained by subjecting each WCE image to scale invariant feature transform (SIFT). A Support vector machine (SVM) classifier is trained with sparse representations of the SIFT and local binary pattern (LBP) features extracted from these key points for bleeding detection.

Existing literature on bleeding detection in WCE images comprises both supervised and unsupervised learning approaches. However, most of the approaches are based on supervised learning due to the complexities involved in unsupervised discrimination of bleeding images. Endoscopic bleeding detection is generally classified as bleeding frame detection and bleeding image detection, depending on the candidate images. Bleeding frame detection refers to the classification of a frame comprising several images from a video sequence as bleeding and non-bleeding. On the other hand, bleeding image detection refers to the analysis of a single discrete image to detect the presence of bleeding.

Irrespective of the temporal characteristics considered in the bleeding frame classification, three approaches are commonly employed in bleeding detection in WCE images. They are called the pixel-based, image-based, and patch-based methods depending on the RoI considered for analysis. The first pixel-based scheme proposed by Hwang et al. [8] is based on the clustering of pixels based on Bayesian classification and expectation maximization clustering. A two-stage scheme proposed by Lau and Correia [9] detects bleeding in the first stage with color saturation parameters of image blocks. The classification results are refined in the second stage with pixel-based analysis of saturation and luminance parameters.

In a pixel-based scheme proposed by Pan et al. [10], each pixel is classified by a probabilistic neural network (PNN) classifier, trained with feature vectors constructed from the RGB and HSV color spaces. A similar approach based on an artificial neural network (ANN) classifier is proposed by

Fu et al. [11]. However, these methods involve heavy computations which linearly increase with the image resolutions. To the contrary, image-based methods employ statistical features extracted from the entire image in bleeding detection. In a kernel-based classifier proposed by Lv et al. [12], local and global feature descriptors comprising color and spatial characteristics are employed in bleeding detection. Yuan et al. [13] proposed a two-stage bleeding detection scheme based on color features extracted from the whole images and *k*-means clustering for grouping the pixels. This approach reportedly achieves best classification accuracy with a SVM classifier trained with features extracted from the YCbCr color space. However, sensitivity of the image-based approaches is low for images with small bleeding regions as reported in [14].

To overcome the limitations of the pixel- and image-based approaches, patch-based methods which extract features from pixel blocks of images are introduced. In these methods, features are extracted from uniformly sized pixel blocks containing local features of the WCE images. In the patch-based approach proposed by Li and Meng [15], WCE images are divided into blocks of 30×30 pixels, and chrominance moments evaluated for each block in the hue-saturation-intensity (HSI) space are employed as features for identification of bleeding regions. In a similar approach proposed by Lee and Yoon [16], the images are divided into blocks of 10×10 pixels from which statistical features extracted are thresholded for bleeding detection. The block-based approach proposed by Gosh et al. [17] in 2018 extracts blocks of pixels separately from the RGB channels and generates a distinct color feature from these blocks for bleeding detection with a K-nearest neighbor (KNN) classifier. Though these approaches are computationally faster compared to pixel-based schemes and are free from pixel randomness issues, their performance and computational time rely on the number of blocks.

Recently, region-based approaches are gaining wide research attention in bleeding detection problems. Bleeding regions are characterized by obscure shapes and in some cases are distributed as varying sized blocks. Region-based methods are very effective in capturing lesions, tumors, bleeding regions, etc. characterized by RoIs of arbitrary shapes and sizes. These regions are extracted from the WCE images with the growcut [18], region growing (RG) [19], and superpixel [20] image segmentation algorithms. Region-based bleeding detection approaches have demonstrated a good degree of accuracy compared to others due to the localization of the RoI for feature extraction.

Inspired by the region-based approaches, in this paper, we present a superpixel-based WCE bleeding detection and segmentation scheme, featuring superior classification and segmentation accuracies. Here, we have exploited the Gaussian mixture model (GMM) superpixels proposed by Ban et al. [21] for bleeding region detection and segmentation of the same from the WCE images. This paper follows a pre-

segmentation-classification-post-segmentation sequence for bleeding detection and precise segmentation of bleeding regions. We have trained an SVM classifier with feature vectors constructed with color and texture attributes extracted from the superpixels for bleeding detection. Experimental results with standard datasets, detailed statistical analyses, comparisons, and interpretations testify the superiority of the proposed system.

The significance of this research is comprehensible from its contributions to the healthcare sector and research community as below.

1. The unexplored GMM superpixels characterized by accurate boundaries are harnessed in the construction of a supervised model for bleeding detection and segmentation, which has never been attempted before.
2. An endoscopic bleeding detection system is realized with dual applications, i.e., classification and bleeding localization by segmentation, with comparatively low computational cost.
3. The proposed system is capable of segmentation of very small and disconnected bleeding regions, attributed to the precision of the GMM superpixels.
4. The proposed system can be optimized for better performance by parallelization of mathematical computations in GMM superpixel construction, which is not supported by other superpixel algorithms.
5. The proposed system featuring high accuracy both in classification and segmentation is an extensible model for diverse medical images for diagnostic and prognostic procedures.

Thus, the proposed system demonstrates its potential for bleeding detection in the contemporary clinical settings and also provides wide scope for extensions to similar medical applications. Furthermore, it also reveals the potential of GMM superpixels, calling for new investigation in their deployment in several image segmentation problems.

The rest of this paper is organized as below. In Section 2, we present a detailed account of existing works in the context of the proposed system. The description of data sets and underlying methodologies are discussed in Section 3 and the architecture of the proposed system is presented in Section 4. Experimental results and comparative analyses are given in Section 5. A discussion on the results is presented in Section 6 and the paper is concluded in Section 7.

2 Related work

This section reviews various superpixel-based bleeding detection schemes for diverse pathologies of the GI tract, revealing their limitations and demonstrating the significance of our

research. A superpixel collectively refers to a group of similar pixels labeled uniquely. They are near complete and semantically similar representations of digital images, providing better trade-offs between computational complexity and under segmentation of images.

The simple linear iterative clustering (SLIC) proposed by Achanta et al. [22] is the most widely used superpixel segmentation algorithm. Fu et al. [20] successfully employed SLIC for bleeding detection in WCE video sequences extracting three color features: red-green ratio, red-blue ratio, and normalized red from the superpixels. An SVM classifier trained with these features demonstrates best classification accuracy with the radial basis function (RBF) kernel function.

Iakovidis [23] proposed a bleeding detection method based on the saliency of superpixels evaluated on color features. It builds the classifier model to identify bleeding regions following a supervised learning approach, on a set of first order statistical measures extracted from various color components of the WCE images.

A three-stage approach for WCE bleeding detection based on superpixels is presented by Xing et al. in [24]. It uses histogram features of the superpixel to distinguish bleeding frames with a KNN classifier. The bleeding regions are further segmented extracting nine features from different color spaces of the superpixels.

In the superpixel-based approach for ulcer detection in WCE images proposed in [25], a saliency map characterizing ulcer regions is constructed from multi-level superpixel representation of images. Locality-constrained linear coding (LLC) is applied on the saliency maps to encode invariant features, histogram gradients, and LBPs of the WCE images to characterize bleeding and non-bleeding regions.

In the superpixel-based approach for detection of polyps on the intestine surfaces proposed by Maghsoudi [26], a SVM classifier is trained with 164 features including color and texture attributes extracted from SLIC superpixels. The system tested with varying numbers of superpixels shows that best classification accuracy is obtained with 100 superpixels.

Choice of discriminating features is very important in bleeding detection, irrespective of the methodology employed for ROI selection. Ratio of red component is an important discerning parameter for bleeding detection. However, WCE images exhibit different shades of red based on the degree of bleeding, time of bleeding, intestinal contents, etc. Several bleeding detection methods exclusively based on color features exist in literature.

Gosh et al. [27] have employed a histogram of maximum block values extracted from a plane of red-green intensity values as a discerning feature for training a KNN classifier for bleeding detection. In [28], Suman et al. have proposed a SVM classifier trained with five color features which achieves a detection accuracy of 97.5% with a RBF kernel. The authors have extended this work in [29] with color, texture, and

combination of color and texture features. Three different classifiers based on random forest (RF), logistic model tree (LMT), and random tree (RT) are trained with a set of 5 color features, 5 best texture features, and 3 combinations of texture and color features. The texture features in each feature set are selected from a complete set of 22 gray level co-occurrence matrix (GLCM) features.

Kundu et al. [30] have proposed a bleeding detection approach with histogram features extracted from the RoI segmented from the normalized RGB color space. A two-stage unsupervised bleeding detection system based on color enhancement is presented in [31]. This paper employs the retinex theory of color perception for color enhancement in the first stage and salient region detection in the second. It is shown that abnormality detection improves with color enhancement.

Segmentation of the RoI in WCE images considerably reduces computational complexity and the size of the feature space. However, selection of RoI itself is very complex in region-based methods based on the heterogeneity of the attributes. RG algorithms are commonly employed in the segmentation of bleeding regions from WCE images for further analysis. These algorithms construct the RoI incrementally starting from a seed pixel or seed region. Sainju et al. [32] proposed a method for bleeding detection based on statistical features extracted from the RoI constructed by RG approach, which requires manual seed selection.

Superpixel-based RG approaches are confronted with the challenges of identification of similar superpixels and sequencing them for integration based on distance measures. In [33], a robust similarity metric and an adaptive superpixel integration strategy are proposed by Chaibou et al. This method defines similarity as a weighted combination of content similarity between superpixels and similarity of boundaries for a seamless integration. In this approach, the superpixels are merged based on agglomerative clustering. A most recent survey by Rahim et al. [34] on the WCE-based GI abnormality detection methods gives a detailed account of various literature pertaining to our research and advocates the need for an integrated mechanism for joint classification of ulcers, polyps and tumors.

From the comprehensive review of various literature, we understand the significances of the region-based approaches for bleeding detection, selection of appropriate features, and segmentation of the RoI. We confine our research to bleeding detection in WCE images based on GMM superpixels, irrespective of the pathologies.

3 Materials and methods

In this section, we present the datasets used in our research and the mathematical background of the underlying methodology.

3.1 Dataset

The dataset 1 includes 3294 WCE images taken from two standard datasets [35, 36]. These images are apportioned in a 50:50 ratio into training and testing datasets. The training dataset contains 686 bleeding and 961 non-bleeding images. The testing dataset contains 487 bleeding images and 1160 non-bleeding images. Both the datasets contain continuous image frames as well as discrete images under both bleeding and non-bleeding categories. We have ensured that the testing data is entirely different from the training data to assess the performance of the system with an arbitrary test data. Furthermore, we have also evaluated the performance of our segmentation process exclusively with dataset 2, available from [18] which contains 50 bleeding samples and 50 non-bleeding samples.

3.2 GMM superpixel

The SLIC [22] algorithm is a kind of clustering-based segmentation algorithm which aggregates pixels in rectangular windows into a superpixel based on the distance measures between color feature vectors and spatial vectors in a five dimensional space. This algorithm defines the pixel windows based on the number of superpixels, a user input L . It limits the number of clusters to L and the pixels are grouped based on their proximity to the centers of these clusters. The SLIC algorithm employs a weight factor to generate superpixels approximately equal in size. Hence, the SLIC superpixels with several isolated heterogeneous regions are not accurate in the segmentation of images.

The GMM superpixels introduced in [21] improve the segmentation accuracies by modeling each superpixel as a Gaussian distribution with unknown parameters. A probabilistic model in which data samples are derived from a mixture of a finite number of Gaussian distributions labeled $l \in \{1, \dots, L\}$, with unknown parameters, is called a Gaussian mixture model. The parameter L refers to the number of clusters into which the data points are distributed. Each Gaussian distribution l is associated with a mean μ_l , a covariance Σ , and the mixing probability π . Given L , the mixing probabilities must satisfy the condition in Eq. (1).

$$\sum_{l=1}^L \pi_l = 1 \quad (1)$$

It is required to perform maximum likelihood estimates (MLM) to determine if the data points are fitted in the respective Gaussians. The probability that an arbitrary data point x belongs to a Gaussian l is expressed by Eq. (2).

$$p(z_l = 1 | x) \quad (2)$$

where z_l is called the latent variable and takes the value 1 when

x belongs to l and 0 otherwise. The mixing coefficient π_l for a Gaussian 1 can be expressed as the probability that a data point belongs to a cluster 1 as in Eq. (3).

$$\pi_l = p(z_l = 1|x) \quad (3)$$

The set of all latent variables can be represented as $z = \{z_1, \dots, z_L\}$. The probability that all the data points belong to the respective clusters is expressed in Eq. (4) and the probability that the data point comes from the cluster l is the Gaussian function given in Eq. (5).

$$p(z) = p(z_1 = 1)^{z_1} p(z_2 = 1)^{z_2} \dots p(z_L = 1)^{z_L} = \prod_{l=1}^L \pi_l^{z_l} \quad (4)$$

$$p(x|z) = \prod_{l=1}^L N(x|\mu_l, \Sigma_l) \quad (5)$$

The probability of z for a given data point x to exist in a Gaussian l is given in Eq. (6).

$$p(z_l = 1|x) = \frac{\pi_l N(x|\mu_l, \Sigma_l)}{\sum_{i=1}^L \pi_i N(x|\mu_i, \Sigma_i)} = \gamma(z_l) \quad (6)$$

From the above equation, the parameters of the model can be determined by expectation maximization (EM). The parameters of the model for a cluster l are collectively represented as $\gamma_l = \{\mu_l, \Sigma_l\}$. GMM superpixels model each pixel as a Gaussian distribution discussed above. Given a 2D image I of dimension $M \times N$, the total number of pixels $P = M \times N$ labeled $p_i \in \{1, 2, \dots, P\}$ can be assigned to a superpixel $l \in \{1, \dots, L\}$ analogous to the clustering of data points into clusters. For any pixel $p_i \in \{1, 2, \dots, P\}$, the superpixel Label l is computed as in Eq. (7).

$$Lb_i = \arg \max_{l \in L} \frac{p(z; \theta_l)}{\sum_{l \in L} p(z; \theta_l)} \quad (7)$$

It is evident that superpixel labels are evaluated based on posterior probability after the evaluation of the unknown parameters γ_l for a cluster l . Influenced by the Gaussian distribution, the pixels are grouped very precisely compared to the SLIC algorithm. We demonstrate this in Fig. 1, which shows the SLIC and GMM superpixel segmentation of a WCE image. It is seen that the homogeneous regions are represented with accurate boundaries with arbitrarily shaped GMM superpixels, whereas they are represented with multiple uniform SLIC superpixels.

4 Proposed system

The proposed system is implemented as a cascade of classification and segmentation processes. The classification is

preceded by pre-segmentation which extracts the ROI. The features for classification of the WCE images are extracted from the ROI to train an SVM classifier. The bleeding images are subjected to post-segmentation for precise segmentation of bleeding regions. The schematic of the proposed system is shown in Fig. 2.

4.1 System architecture

The four phases of the proposed system are described in the following subsections.

4.1.1 Preprocessing

The images captured in the WCE process are prone to uneven brightness distribution due to the orientation of light sources, resulting in visual degradations. Since the proposed method is based on color features, we perform a decorrelation stretching operation on the images to enhance the differences in colors. This operation is based on correlation operation on the Eigen decomposition of the correlation matrices of the color channels.

4.1.2 Pre-segmentation

This process segments the ROI from the WCE image for feature extraction. Since we are concerned with the bleeding region, we eliminate the green colored components from the WCE images. It is performed by segmenting the WCE image into GMM superpixels and eliminating the pixels with green intensity values greater than 80. Empirical studies on color models have shown that a pixel with a green intensity greater than 80 cannot have a red hue. This pixel level segmentation in each superpixel results in elimination of green components completely, which may not be eliminated, considering the mean green component of the superpixels. The superpixels are then grouped together to form the composite RGB image which is the resultant ROI free from green components. This process is illustrated with Fig. 3. The pre-segmentation algorithm is as below.

4.1.3 Classification

The training and testing images are subjected to pre-segmentation as described in the previous subsection and features are extracted from these images to construct feature vectors for training the SVM classifier. The features employed in bleeding detection are listed in Table 1.

A feature vector comprising the seven features $\{f_1, f_2, f_3, f_4, f_5, f_6, f_7\}$ is constructed from each training and testing image. These features are selected based on our empirical studies and existing literature. The feature f_1 called the *Excess Red* is a representation of the red component excluding the green component. This feature captures the red component of a candidate

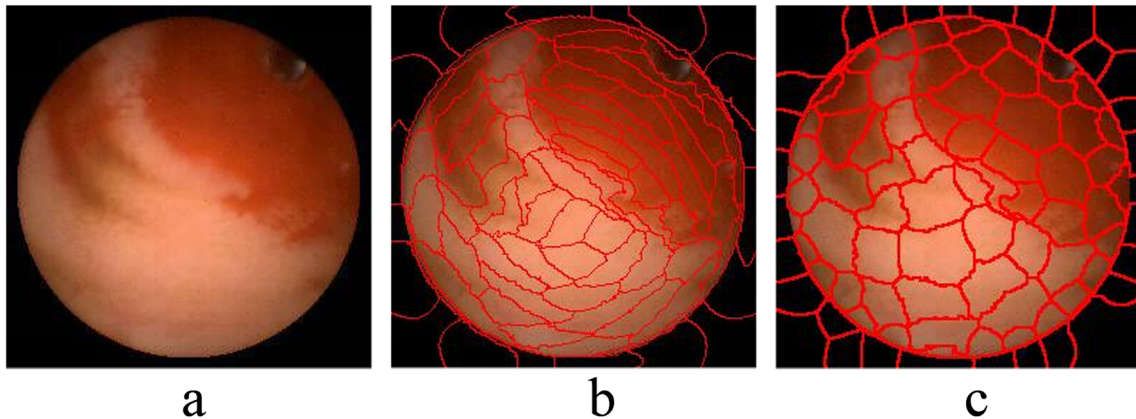


Fig. 1 Superpixel segmentation

image eliminating the green component. The feature f_2 is the proportion of the red component compared to the green component which determines the dominant component among them. Similarly, f_3 is a measure of the proportion of red and blue components. The feature f_4 called *chromaticity* is a measure for clearly distinguishing red regions. It is higher for bleeding regions compared to non-bleeding regions. The features f_2 , f_3 , and f_4 are employed in [29] for color-based segmentation and also in color- and texture-based segmentation. In addition to these color

features, we have also employed three GLCM features. The *entropy* f_5 is a measure of the randomness of the pixels. This measure is higher for large bleeding regions compared to smaller and non-bleeding regions. The *contrast* f_6 is a discriminating feature which is higher for bleeding images compared to non-bleeding images. The *Energy* feature f_7 is a measure of the uniformity or homogeneity of the image. A homogenous image is characterized by few gray levels compared to a highly textured image. The contrast of an image decreases with the homogeneity.

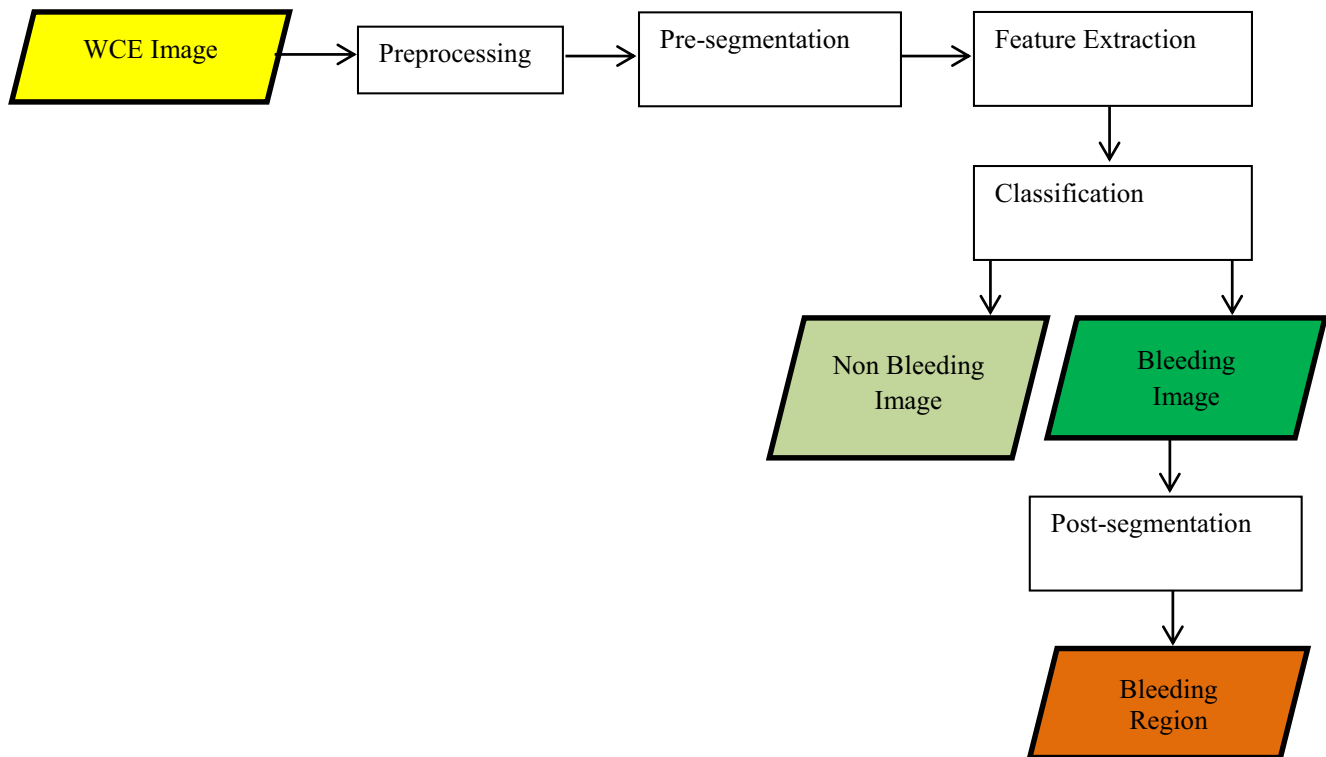
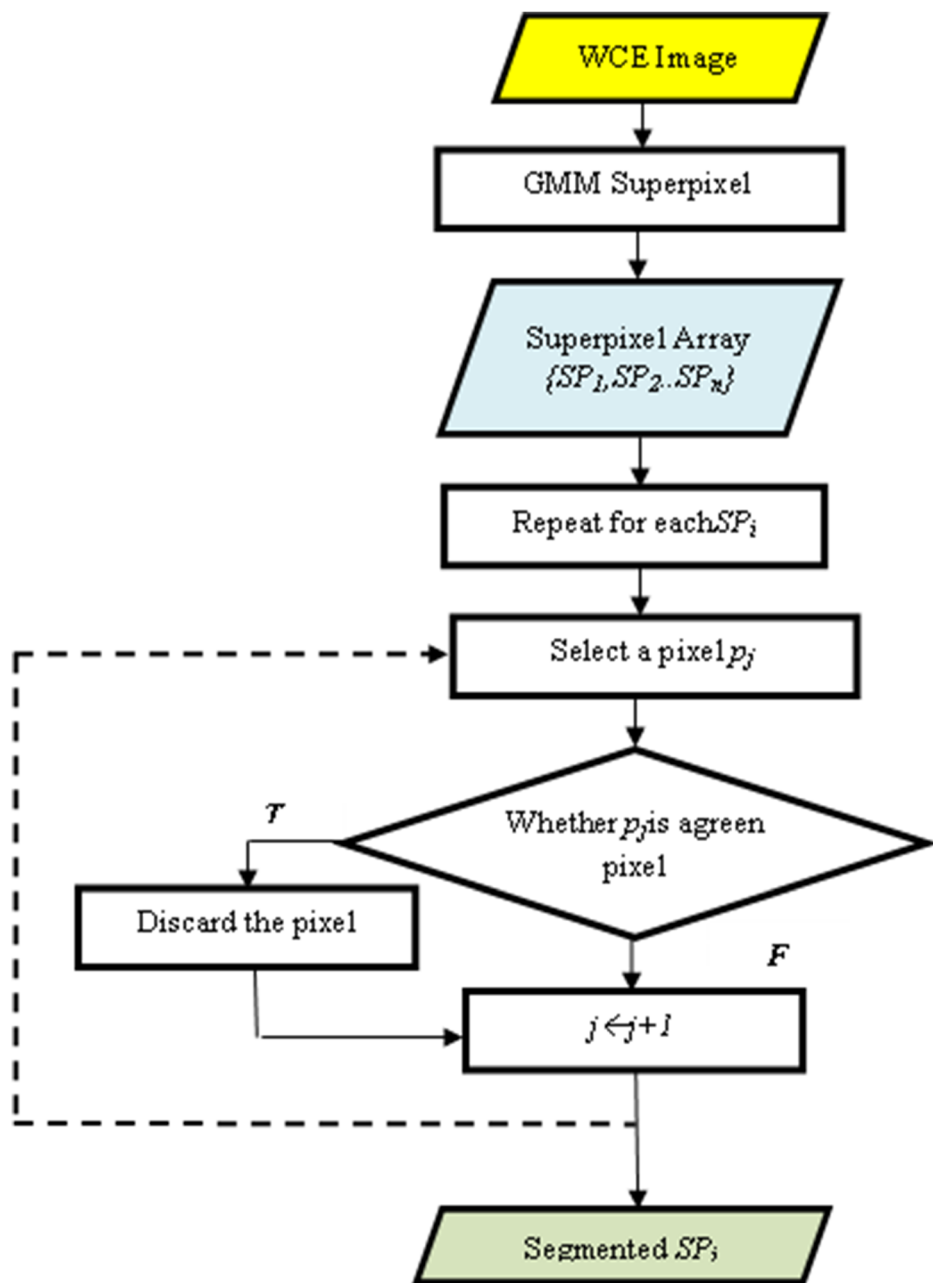


Fig. 2 System architecture

**Fig. 3** Pre-segmentation

On testing, features vectors representing the testing images are fed as input to the SVM classifier and the responses of the classifier are captured.

4.1.4 Post-segmentation

This process is performed to capture the bleeding regions precisely as shown in Fig. 4. It is performed on the segmented superpixels of the WCE images generated during pre-segmentation which contain the RGB components

characterizing active and early bleeding regions. This process begins with assigning a color label to each superpixel based on the means of the red, green, and blue channels. We have identified a set of nine color shades {"red," "orange," "brown," "maroon," "purple," "pink," "red orange," "mahogany," "brown," "bittersweet"} characterizing different types of bleeding. Each superpixel is assigned one of these labels if it contains a bleeding region. Followed by this, the labeled superpixels are merged to segment the bleeding regions. Initially, one of these labeled superpixels possessing the

Table 1 Features extracted from pre-segmented images

Feature ID	Feature	Mathematical expression	Description
	Normalized red mean	$\bar{R}_N = \frac{\bar{R}}{\bar{R} + \bar{G} + \bar{B}}$	Normalized mean of red pixel intensities $\bar{R} = \sum_{m,n} R_i$ $\bar{G} = \sum_{m,n} G_i$ $\bar{B} = \sum_{m,n} B_i$
	Normalized green mean	$\bar{G}_N = \frac{\bar{G}}{\bar{R} + \bar{G} + \bar{B}}$	Normalized mean of green pixel intensities
f_1	Excess red	$EXR = 1.4 * \bar{R}_N - \bar{G}_N$	Additional red component
f_2	Red-green ratio	$RG = \bar{R}/\bar{G}$	Ratio of red and green component
f_3	Red-blue ratio	$RB = \bar{R}/\bar{B}$	Ratio of red and blue component
f_4	Chromaticity	$Ch = 1 - \min(\bar{G}, \bar{B})/\bar{R}$	
f_5	Entropy	$En = - \sum_{i=0}^{n-1} p_i^i \log_b p_i^i$	Measure of randomness of pixels n —number of gray levels
f_6	Contrast	$\sum_{i,j=0}^{N-1} P_{ij}(i-j)^2$ P_{ij} is the pixel at position i,j	Local variations in the GLCM of image
f_7	Energy	$E = \sum_{i,j=0}^{N-1} P_{ij}^2$	Measure of uniformity of image

highest mean red component is selected as a seed and the deltaE value is computed between the seed and the other labeled superpixels. The deltaE measure which quantifies the similarity between colors signifies imperceptible and perceptible differences between two colors. We define a threshold θ_E to control the merging of superpixels. Though the color descriptors are defined for bleeding regions, we found from empirical results that the superpixels of the non-bleeding regions are also labeled “maroon” or “brown.” We prevent these superpixels from being grouped with bleeding superpixels with θ_E . The post-segmentation process is given in Algorithm 2.

5 Experimental results and comparative analyses

5.1 Classification results

The proposed system is implemented in Matlab 2017, trained, and tested with a Intel Core i5 processor with 32 GB RAM. The description of the training and testing dataset for classification is given in Table 2.

We show the results of pre-segmentation of images prior to feature extraction in Fig. 5. It is seen that the bleeding regions in the second and third columns are very

clear after contrast enhancement and noticeable changes are not evidenced in the non-bleeding image in column 1. Also, the superpixels are accurately defined and elimination of the green component from these images segregates the susceptible bleeding regions. It is obvious that features extracted from these regions are sufficient for feature extraction.

The binary SVM classifier is trained with the feature vectors containing seven features, constructed from each of the pre-segmented training image. The resultant learning model is tested with the feature vectors of test images. The classification results obtained with this model for dataset 1 are shown in the confusion matrix in Fig. 6.

From Fig. 6, it is seen that there are 2 misclassifications of non-bleeding images, while the classification of bleeding regions is accurate. The high classification accuracy of the system is attributed to the feature vectors which clearly discern the bleeding and non-bleeding regions. The misclassifications are shown in Fig. 7 for a visual analysis. It is seen from these results that there is no obvious change in the images due to contrast enhancement. The misclassification of these samples is attributed to the labeling of the non-bleeding superpixels as “brown.”

We compare the classification results of the proposed classifier with that of similar bleeding detection systems in Table 3, with the performance metrics evaluated with the

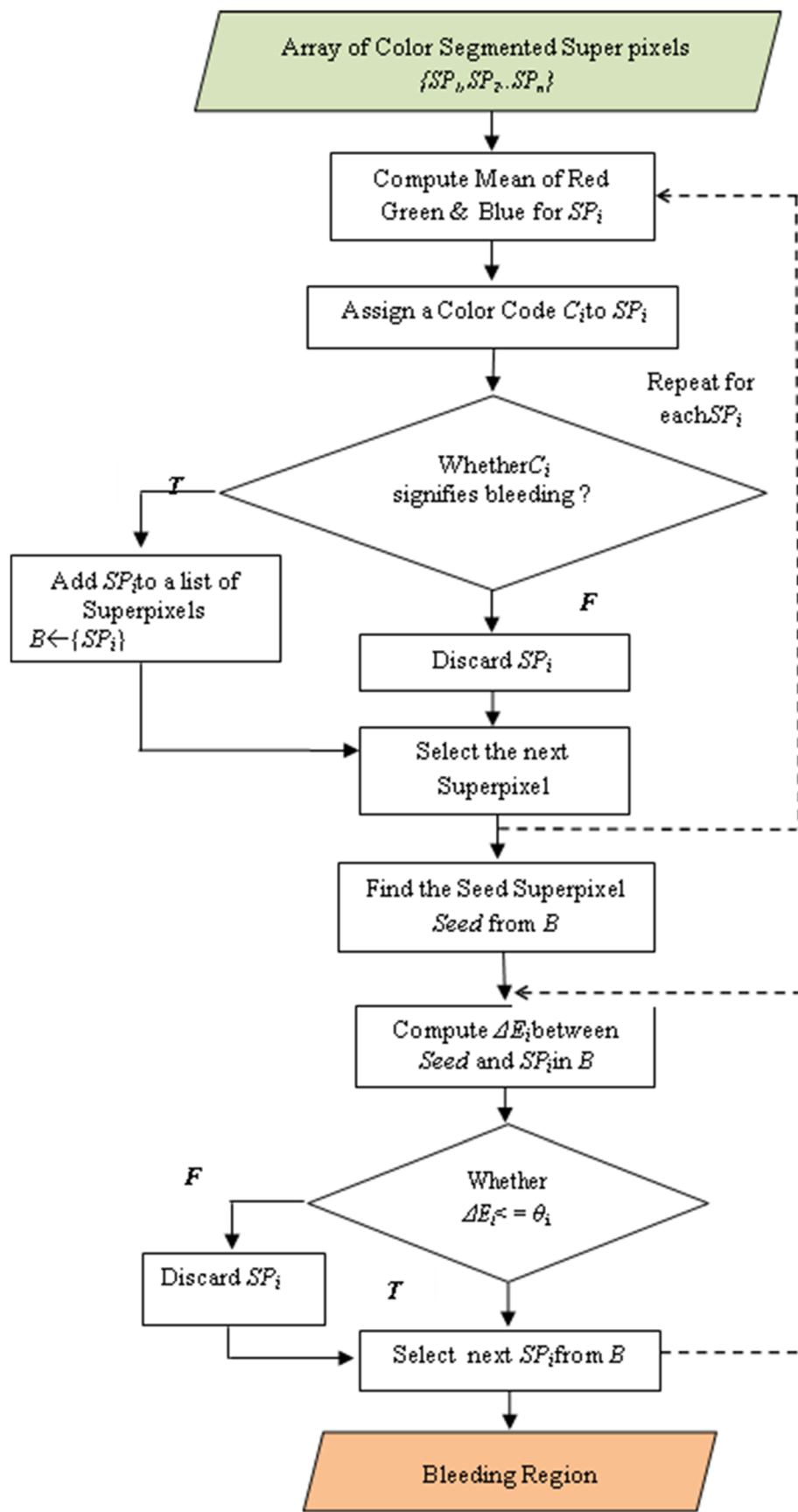


Fig. 4 Bleeding region segmentation

Table 2 Training and test data description

Image type	Total no. of images	No. of training images	No. of testing images
Bleeding	1647	686	1160
Non-bleeding	1647	961	487

equations from (8)–(11).

$$\text{Sensitivity} = \text{TP}/(\text{TP} + \text{FN}) \quad (8)$$

$$\text{Specificity} = \text{TN}/(\text{TN} + \text{FP}) \quad (9)$$

$$\text{Accuracy} = (\text{TP} + \text{TN})/(\text{TP} + \text{TN} + \text{FP} + \text{FN}) \quad (10)$$

$$\text{Precision} = \text{TP}/(\text{TP} + \text{FP}) \quad (11)$$

where TP is true positive, TN is true negative, FP is false positive, and FN is false negative.

It is seen that the proposed approach exhibits best performance metrics compared to other systems. The area under curve (AUC) generated for the proposed classifier with the Classifier Learner App is shown in Fig. 8. Due to the accuracy of classifications, the AUC

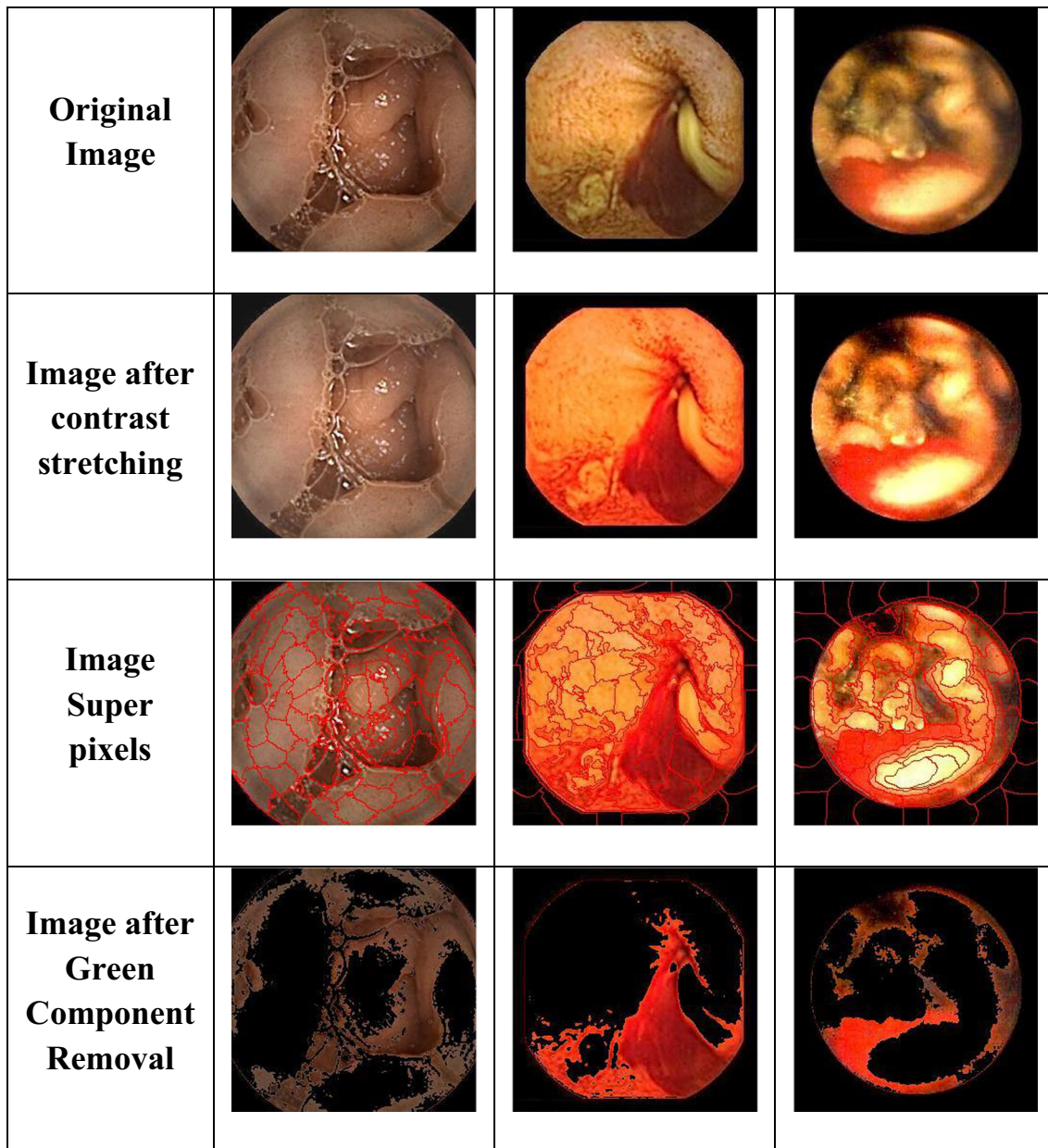
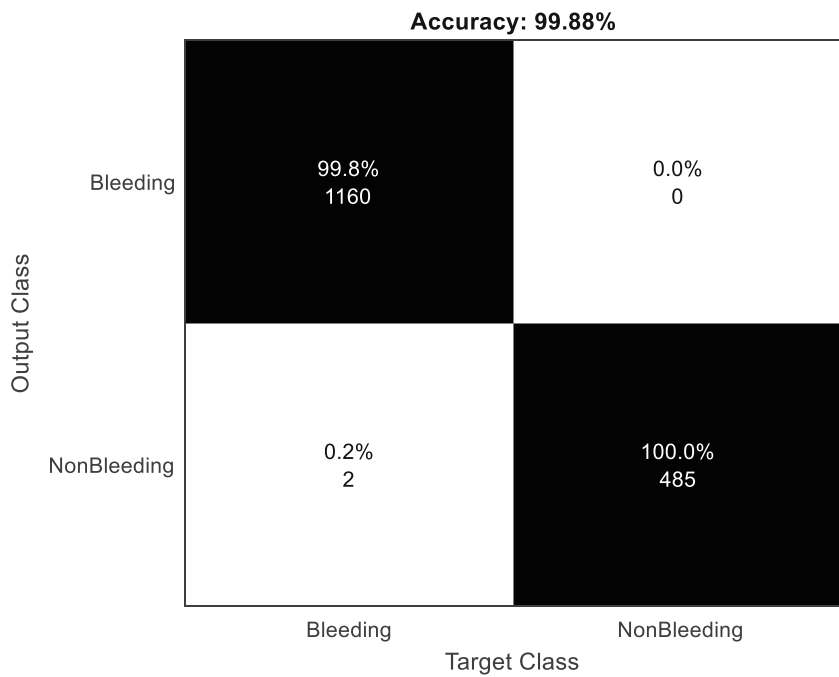
**Fig. 5** Pre-segmentation

Fig. 6 Confusion matrix-bleeding detection



evaluates to 100 which complements the classification accuracy.

5.2 Segmentation results

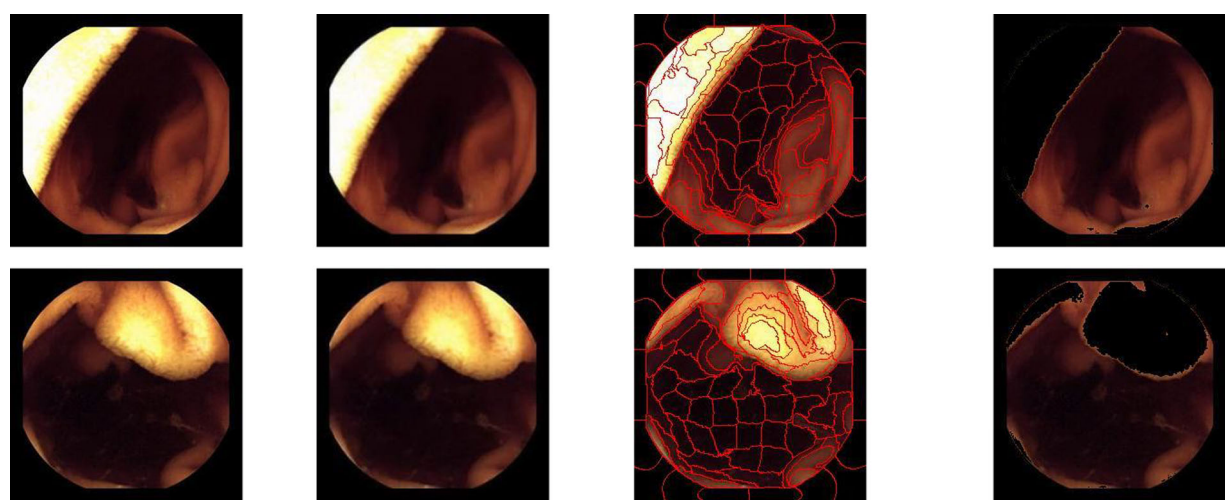
In this section, we present the results for segmentation of the bleeding regions. To demonstrate the efficacy of the segmentation process, some of the exemplary results for dataset 1 and dataset 2 are shown in Figs. 9, 10 respectively. The test samples shown here are characterized by bleeding regions of varying sizes and different bleeding color shades taken from the

two datasets. We see that the segmented regions match with the corresponding ground truths.

The quantitative metrics to evaluate the segmentation process are given in Table 4. The Dice Score and the Jaccard Index which measure the overlap between the mask of the segmented image and the ground truth are evaluated with Eqs. (12) and (13).

$$\text{Dice Score} = 2\text{TP}/(2\text{TP} + \text{FP} + \text{FN}) \quad (12)$$

$$\text{Jaccard Index} = \text{TP}/(\text{TP} + \text{FP} + \text{FN}) \quad (13)$$



Original Image **Image after contrast stretching** **Image Super pixels** **Image after Green component Removal**

Fig. 7 False positives

Table 3 Performance comparison for classification

Classifier	Accuracy	Specificity	Sensitivity
Proposed method	99.88 ± 0.0030	1 ± 0.0001	99.83 ± 0.0060
Patel et. al. [7]	99.18	Not reported	98.00
Deeba et al. [19]	94.5	95.07	92.32
Kundu et al. [30]	97.86	95.20	98.32
Pogorelov Et al. [29]	97.7	95.5	97.6
Yuan et al.[13]	91.96	98.7	97.15

It is seen that the segmentation performance metrics are best for dataset 1 compared to that of dataset 2. The overlap scores also testify the similarity of the segmented images and the ground truth. The lower values are attributed to the appearance of false positives in our segmentation results as in Fig. 10.

On a thorough analysis of the misclassified samples, we identified both bleeding and non-bleeding superpixels labeled “maroon” and “brown.” For definition of colors, we have followed the copyrighted Matlab code of Stephen Cobeldick [37] for mapping RGB values to colors. We have computed the value of θ_E adaptively for each image, defining the nearness of Δ_E to the mean red component of each superpixel. Some of our segmentation results not matching the ground truth for dataset 1 and dataset 2 are shown in Fig. 11.

We see that the original images in this figure are low contrast images with poor contrast between the foreground and background. However, by modifying the θ_E values, we get better segmentation results for the test images in rows 3 and 4 of the above figure as in Fig. 12.

From the above results, it is seen that the classifier exhibits best performance in the detection of bleeding images with a small feature set compared to other bleeding detection systems. However, segmentation of low contrast images with

small bleeding regions which are not discernable from the background introduce noisy pixels in the segmented images.

It has been established that two colors for which Δ_E values range from 0 to 2 are visually indistinguishable. However, in the proposed system Δ_E values between different shades of red and the dominant red in a superpixel cannot be clearly defined. Hence, we introduce θ_E to selectively group the superpixels. Compared to the conventional RG algorithms based on Euclidean distances between centroids of manually selected seed points, in this system, the seed superpixel and θ_E are adaptively chosen by empirical evaluation from the respective bleeding images.

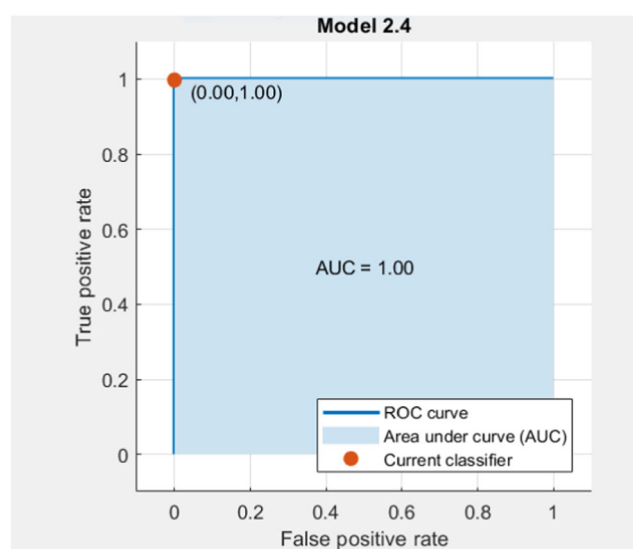
Comparison of segmentation algorithms is very challenging due to the diversities of datasets and methods employed, each of them influencing the performance of the system. In addition to the quantitative metrics, the various aspects of implementation must be considered to evaluate the performance of the bleeding detection systems. We present a summary of the state-of-the-art approaches and the proposed system in Table 5 for a fair comparison.

From the above, it is seen that best accuracy is achieved with a smaller feature set with our system. Though a matching performance is reported in the work of Deeba et al. [19], their method extracts features from the RGB and HSV spaces and uses two SVM classifiers and fuses their results for classification with a third SVM. In the work of Pogorelov et al. [29], several analyses are presented based on color features, texture features, and their combinations, tested with several classifiers. This table contains the performance statistics obtained with this method with minimum number of features. Similarly from Kundu et al. [30], we have taken the best results obtained irrespective of the number of bins. Yuan et al. [13] employ two classifiers trained on an 80-word color feature. The approach proposed in [7] is computationally expensive compared to the other approaches as it involves sparse coding of SIFT and uniform LBP descriptors.

Computational time is a significant metric which depends upon the feature vector size and cost of mathematical operations, signifying the performance of the system. We present a comparison of computational cost of our method with that reported in the work of Deeba et al. [19] and Patel et al. [7] in Table 6.

In [19], the authors have reported only the classification time for the three types of classifications where C_{rgb} and C_{hsv} are SVM classifiers trained on features of the RGB and HSV spaces respectively. Similarly, C_{fusion} is an SVM classifier which classifies the frame based on the outputs of C_{rgb} and C_{hsv} . In the proposed system, we consider both discrete and continuous WCE images. The computational cost given in Table 6 is the average of the training and testing costs. We see that these costs are very low for the proposed system.

The conventional accuracy, specificity, sensitivity, and precision measures are not reliable in classification problems where the size of the classes is different. Hence Matthews correlation coefficient (MCC) and F1 score, called balanced measures, are used in the binary classification problems. The

**Fig. 8** Area under curve

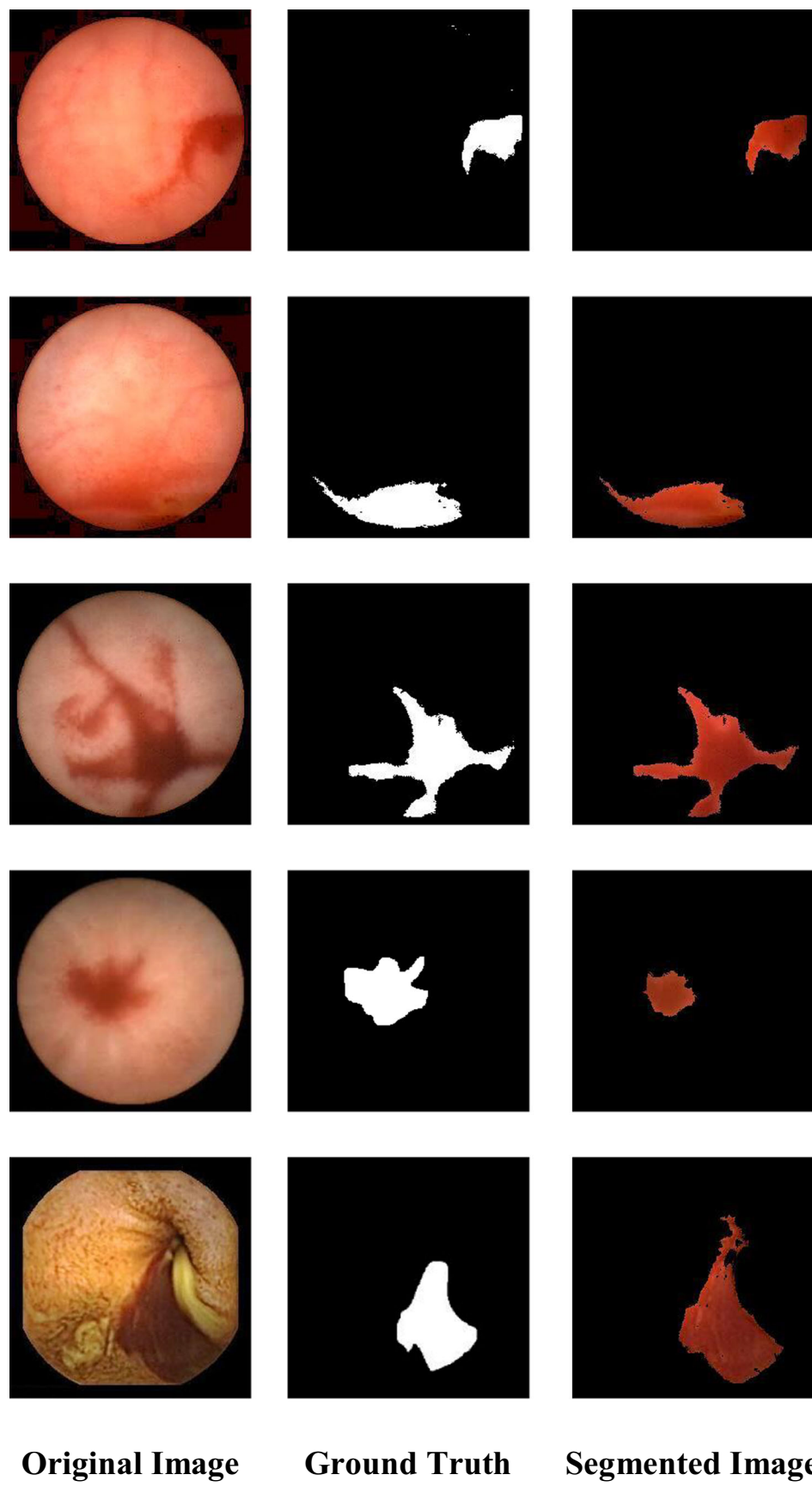


Fig. 9 Segmentation of bleeding regions—dataset 1

F1 score is evaluated to find the balance between precision and sensitivity of the system. It is very well known that precision is the ratio of the number of positive predictions out of the total number of positive predictions by the system. Sensitivity is the ratio of the number of positive predictions to the total number of positive input samples. The F1 score is the weighted average of these measures ranging from 0 to 1.

MCC ranging from -1 to $+1$ is considered to be more informative than F1 as it is based on the balanced ratios of TP,

FP, TN, and FN values. The F1 and MCC measures are evaluated with Eqs. (14) and (15).

$$F1 = \frac{2 * (\text{Recall} * \text{Precision})}{(\text{Recall} + \text{Precision})} \quad (14)$$

$$MCC = \frac{TP \times TN - FP \times FN}{\sqrt{(TP + FP)(TP + FN)(TN + FP)(TN + FN)}} \quad (15)$$

Fig. 10 Segmentation of bleeding regions—dataset 2

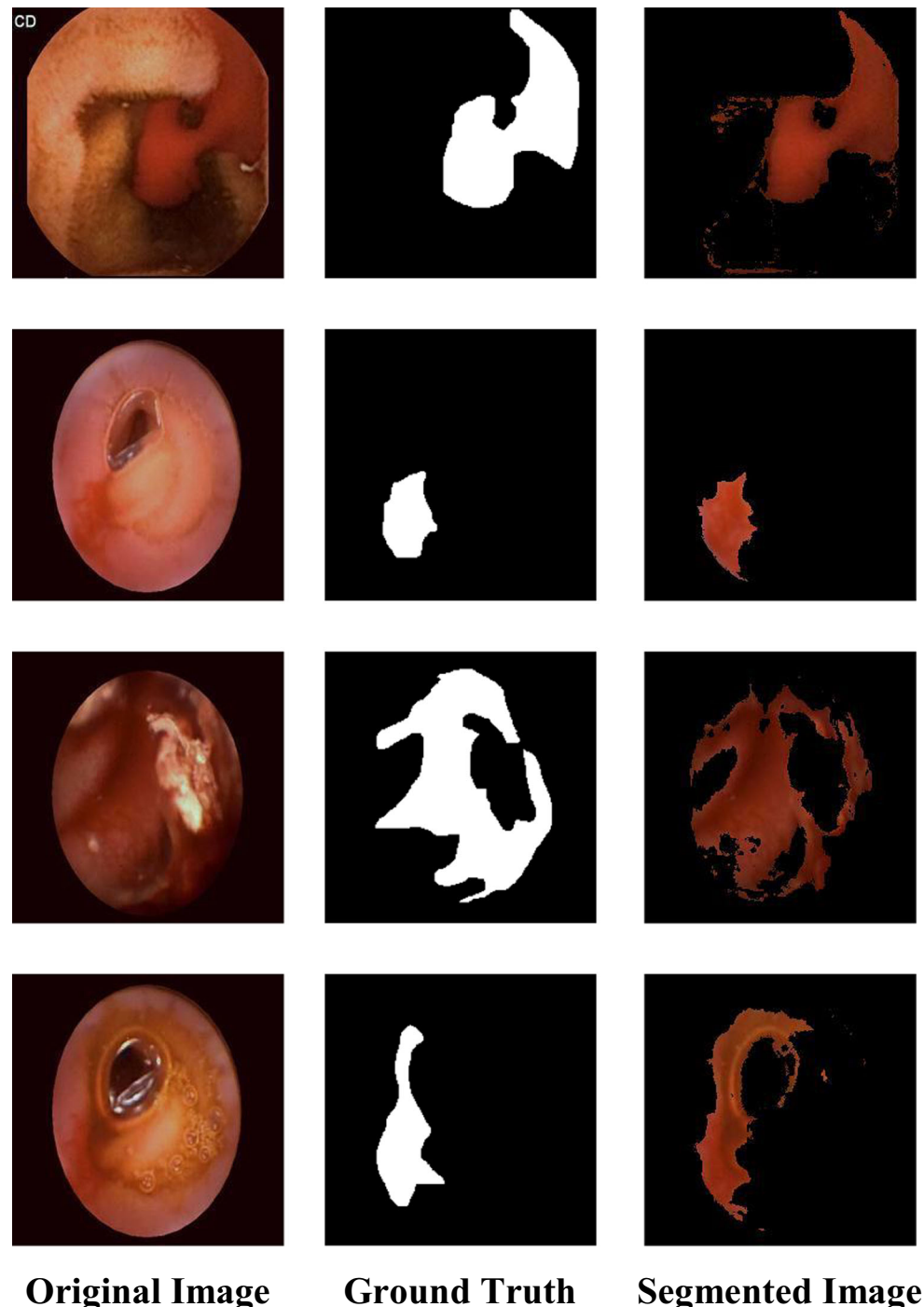


Table 4 Performance metrics for segmentation

Dataset	Accuracy	Specificity	Sensitivity	Precision	Dice Score	Jaccard Index
1	0.9959 ± 0.0023	0.9987 ± 0.0015	0.9849 ± 0.0128	0.9963 ± 0.0032	0.9928 ± 0.0079	0.9858 ± 0.0143
2	0.9961 ± 0.0013	0.9965 ± 0.0023	0.9345 ± 0.0121	0.9909 ± 0.0045	0.9905 ± 0.0059	0.9813 ± 0.0114

With respect to these measures, we present a comparison of our system with that of three SVM classifiers with different kernels in Table 7.

It is observed from Table 7 that the proposed binary SVM classifier is very accurate compared to other SVM classifiers for bleeding detection, irrespective of the distribution of samples in test dataset. From the above extensive experimental results and comparisons, we have established the superiority of our system with respect to classification and segmentation.

6 Discussions

From the performance evaluations and comparative analyses, the proposed bleeding detection system is demonstrated to be superior to the state-of-the-art approaches. It is understood from Table 5 that the method of Deeba et al. [19] demonstrates a classification accuracy of 99.6% which closely matches the classification accuracy of the proposed system. However, the authors employ an

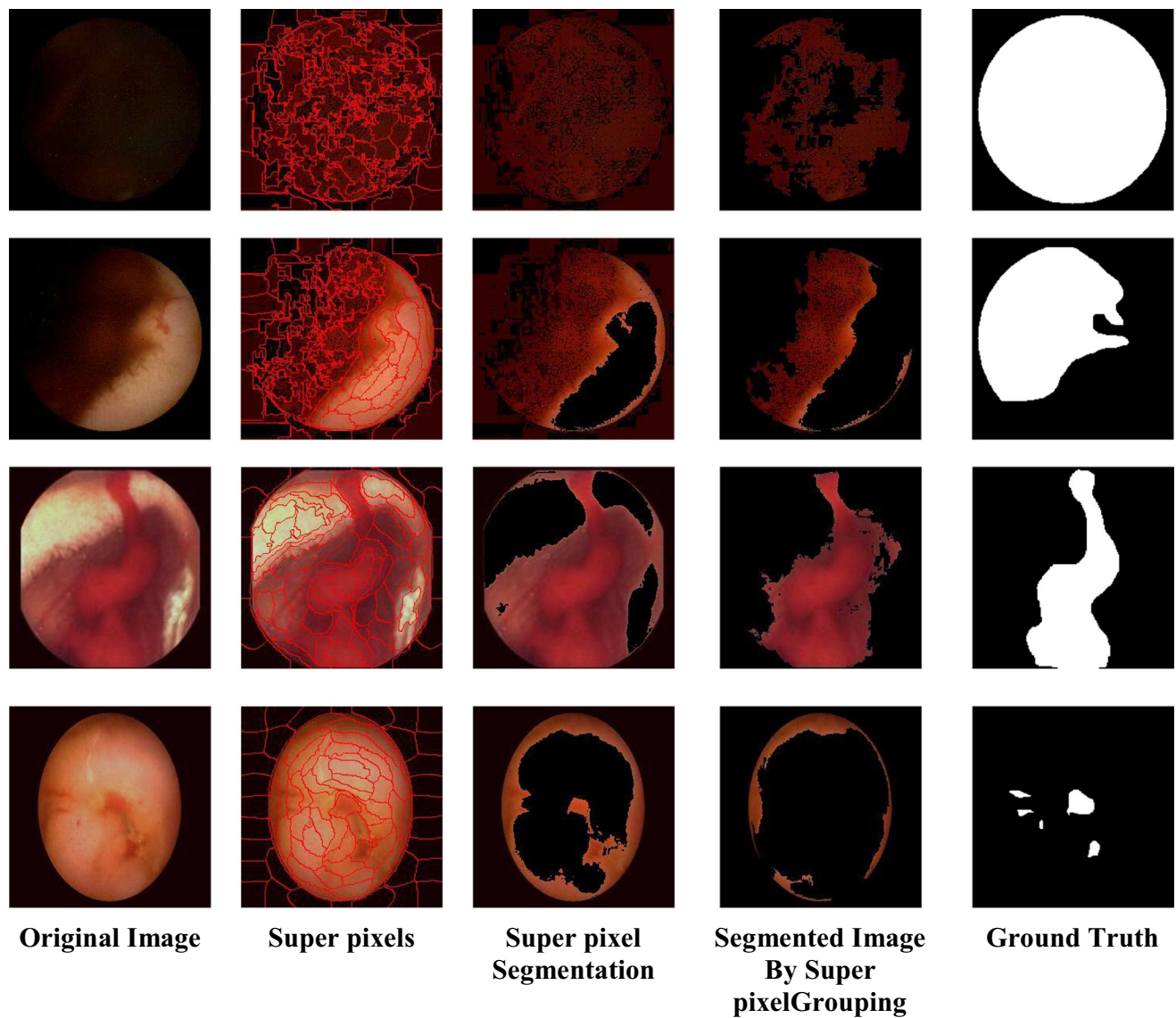
**Fig. 11** Segmentation errors

Fig. 12 Segmentation results with modified θ_E



exhaustive feature set from the RGB and HSV spaces and three SVM classifiers for bleeding detection. The approach proposed in [13] demonstrates a comparable classification accuracy of 98.05%. Nevertheless, it employs a set of 80-bin color histogram features from the RGB space for training the SVM classifier. Similarly, the approach proposed in [30] achieves a classification accuracy of 97.86% with 64 histogram features extracted from the RGB space. The lowest classification accuracy of 93.4% is reported in [29] for a set of 5 color features with a Random Tree classifier. The most recent method based on sparse coding proposed in [7] constructs feature vectors by SIFT and LBP operations on the RoI obtained by SIFT transform of the image achieving an accuracy of 98.18%, for a dictionary size of 300. These results show that the proposed model achieves best accuracy with a SVM classifier trained with optimal features.

Though the proposed model is demonstrated to be superior to the state-of-the-art approaches, a more reliable performance analysis can be performed with cross-validation results obtained from different SVM classifiers built with different kernels. This operation is performed with the Classifier Learner App in Matlab 2017b with a 10-fold cross validation on the test data. The cross-

validation results are given in Table 8 for the linear SVM classifier employed in the proposed system and four other SVM variants.

Generally, a linear SVM classifier maps the data points with a linear kernel into a high-dimensional space and finds an optimal hyperplane separating the data points of the classes. A quadratic SVM defines a decision boundary with a quadratic kernel, which is a case of the polynomial kernel of dimension 2. This SVM separates the data points based on their similarity and interactions between them. A Gaussian SVM separates the data points with a Gaussian kernel based on the Euclidean distance between them. This kernel evaluates to 1 when the data points are highly similar, i.e., very close in the high-dimensional space. Variants of Gaussian SVM such as fine Gaussian SVM, medium Gaussian SVM, and coarse Gaussian SVM are introduced defining different kernel scale parameter in each type, based on the number of predictor variables. While the fine SVM makes a fine distinction between the classes, the coarse SVM makes a rough distinction and the medium SVM makes medium distinctions based on a third order polynomial.

The cross-validation results in Table 8 show that best classification accuracy is obtained by quadratic and medium Gaussian SVMs. However, the accuracy of the linear

Table 5 Summary of state-of-the-art bleeding detection schemes

Classifier	Bleeding detection method	Feature set	Accuracy
Proposed Method	GMM superpixel + color features + texture features + SVM	Excess red, red-green ratio, red-blue ratio chromaticity, entropy, contrast, energy	99.88 ± 0.0030
Patel et al. [7]	Sparse coding SVM	SIFT + uniform LBP	98.18
Deeba et al. [19]	Color features+ HSV features + 3 SVM classifiers	Mean (R), mean (G), standard deviation (G) Mean(H), mean (S), mean (V), standard deviation (S)	99.6
Kundu et al. [30]	RGB histogram + KNN	64 histogram frequencies from RGB channels	97.86
Pogorelov et al.[29]	Color + random tree	Red-green ratio, red-blue ratio, normalized red, ratio of the red channel to vector amplitude of the green and blue channels, chromaticity	93.4
Yuan et al. [13]	Color histogram + KNN + SVM	80-bin word color histogram features	98.05

Table 6 Computational time

Method	Classifier	Training time	Classification time
Proposed method	SVM	9.7225e-04 s/image	2.6736e-05 s/image
Patel et al.[7]	SVM	Not reported	2 s/image
Deeba et al. [19]	C_{rgb}	Not reported	0.0924 s/frame
	C_{hsv}	Not reported	0.1584 s/frame
	C_{fusion}	Not reported	0.2145 s/frame

SVM is lower by only 0.02% compared to these SVMs. These analogous results reinforce the stability of the SVM classifiers with respect to the feature set employed in training them. This further signifies the effectiveness of the GMM superpixels in the semantic segmentation of WCE images. Furthermore, the quadratic and medium Gaussian SVMs are highly complex compared to the linear SVM, owing to the computations involved in discriminating the data points.

The performance metrics for classification and segmentation are expressed with the standard deviations in Tables 3, 4, 7, and 8. It is observed that the metrics tend to be closer to the mean values with a small spread which signifies the stability of the proposed framework for arbitrary test data. It is seen from Table 4 that the standard deviations are higher for sensitivity and Jaccard Index for segmentation in both datasets. This shows that detection of false positives and true negatives by the segmentation model needs improvement, which can be achieved by considering the subtle variations in colors to discriminate bleeding and non-bleeding regions.

Finally, it is evident that the proposed system performs segmentation of the bleeding regions and bleeding detection with high accuracies and low computational complexities. The pipeline of the bleeding detection framework is very promising for classification and segmentation tasks in endoscopic imaging-based treatment of GI pathologies. This is ascribed to the elimination of the trivial regions which do not possess sufficient details for the clinical examination of the endoscopic images.

Table 7 Performance metrics with state-of-the-art SVM classifiers

Method	Classifier	F1	MCC
Proposed method	SVM	0.9991 ± 0.0021	0.9971 ± 0.0029
	Linear		
Pogorelov et al. [29]	SVM	0.949	0.860
	Linear		
	SVM	0.962	0.868
	Polynomial		
	SVM	0.978	0.898
	RBF		

Table 8 Cross-validation results

Classifier	Accuracy
Linear SVM (proposed method)	99.88 ± 0.0030
Quadratic SVM	99.9 ± 0.0042
Fine Gaussian SVM	99.8 ± 0.0027
Medium Gaussian SVM	99.9 ± 0.0061
Coarse Gaussian SVM	99.8 ± 0.0072

7 Conclusion

This paper proposes a novel bleeding detection system for WCE images based on GMM superpixels and SVM. The performance of this system is testified with extensive experimental works on standard datasets and comparative evaluations with state-of-the-art approaches. The proposed system employs a feature set with seven attributes and demonstrates 99.88% accuracy, 99.83% sensitivity, and 100% specificity which are superior to that of state-of-the-art models. The representative state-of-the-art methods which extract features by sparse coding, SIFT, and color histograms from the RGB and HSV spaces are computationally expensive compared to the extraction of seven features from the superpixels of the pre-segmented images, in the proposed system. The classification and segmentation accuracies of the proposed model are attributed to the GMM superpixels which clearly define the boundaries of homogenous regions of the WCE images. This model has also resulted in a few misclassifications and obscure segmentations which can be improved by incorporating more number of color definitions of bleeding regions with unique color vectors, accommodating more number of diverse shades of bleeding regions. This can yield better results for bleeding detection with color features exclusively. This paper opens new avenues for research in color-based segmentation and extending the applications of GMM superpixels in medical image segmentation problems. The simplicity and efficacy of our system makes it a potential solution for clinical trials for improved interpretations of WCE images.

References

- Iddan G, Meron G, Glukhovsky A, Swain P (2000) Wireless capsule endoscopy. *Nature* 405(6785):417
- Robertson KD, Singh R (2019) Capsule endoscopy. In StatPearls [Internet]. StatPearls Publishing
- Hwang S, Oh J, Cox J, Tang SJ, Tibbals HF (2006) Blood detection in wireless capsule endoscopy using expectation maximization clustering. In Medical Imaging 2006: Image Processing. International Society for Optics and Photonics 6144:61441P
- Lau PY, Correia PL (2007) Detection of bleeding patterns in WCE video using multiple features. In 2007 29th Annual International

- Conference of the IEEE Engineering in Medicine and Biology Society (pp. 5601–5604). IEEE
- 5. Liu Q, Liu Z, Yong S, Jia K, Razmjoo N (2020) Computer-aided breast cancer diagnosis based on image segmentation and interval analysis. *Automatika* 61(3):496–506
 - 6. Prasath VS, Thanh DN, San NQ, Dvoenko S (2020) Human visual system consistent model for wireless capsule endoscopy image enhancement and applications. *Pattern Recognit Image Anal* 30(3): 280–287
 - 7. Patel A, Rani K, Kumar S, Figueiredo IN, Figueiredo PN (2020) Automated bleeding detection in wireless capsule endoscopy images based on sparse coding. *Multimedia Tools and Applications*, 1–14
 - 8. Hwang S, Oh J, Cox J, Tang SJ, Tibbals HF (2006) Blood detection in wireless capsule endoscopy using expectation maximization clustering. In: *Medical Imaging 2006: Image Processing* (Vol. 6144, p. 61441P). International Society for Optics and Photonics
 - 9. Lau PY, Correia PL (2007) Detection of bleeding patterns in WCE video using multiple features. In: *2007 29th Annual International Conference of the IEEE Engineering in Medicine and Biology Society* (pp. 5601–5604). IEEE
 - 10. Pan G, Yan G, Qiu X, Cui J (2011) Bleeding detection in wireless capsule endoscopy based on probabilistic neural network. *J Med Syst* 35(6):1477–1484
 - 11. Fu Y, Mandal M, Guo G (2011) Bleeding region detection in WCE images based on color features and neural network. In: *2011 IEEE 54th International Midwest Symposium on Circuits and Systems (MWSCAS)* (pp. 1–4). IEEE
 - 12. Lv G, Yan G, Wang Z (2011) Bleeding detection in wireless capsule endoscopy images based on color invariants and spatial pyramids using support vector machines. In: *2011 Annual International Conference of the IEEE Engineering in Medicine and Biology Society* (pp. 6643–6646). IEEE
 - 13. Yuan Y, Li B, Meng MQH (2015) Bleeding frame and region detection in the wireless capsule endoscopy video. *IEEE J Biomed Health Inform* 20(2):624–630
 - 14. Iakovidis DK, Koulaouzidis A (2015) Software for enhanced video capsule endoscopy: challenges for essential progress. *Nat Rev Gastroenterol Hepatol* 12(3):172–186
 - 15. Li B, Meng MQH (2009) Computer-aided detection of bleeding regions for capsule endoscopy images. *IEEE Trans Biomed Eng* 56(4):1032–1039
 - 16. Lee YG, Yoon G (2011) Real-time image analysis of capsule endoscopy for bleeding discrimination in embedded system platform. *World Acad Sci Eng Technol* 59:2526–2530
 - 17. Ghosh T, Fattah SA, Wahid KA (2018) CHOBS: color histogram of block statistics for automatic bleeding detection in wireless capsule endoscopy video. *IEEE J Trans Eng Health Med* 6:1–12
 - 18. Deeba F, Bui FM, Wahid KA (2016) Automated growcut for segmentation of endoscopic images. In: *2016 International Joint Conference on Neural Networks (IJCNN)* (pp. 4650–4657). IEEE
 - 19. Deeba F, Islam M, Bui FM, Wahid KA (2018) Performance assessment of a bleeding detection algorithm for endoscopic video based on classifier fusion method and exhaustive feature selection. *Biomed Signal Process Control* 40:415–424
 - 20. Fu Y, Zhang W, Mandal M, Meng MQH (2013) Computer-aided bleeding detection in WCE video. *IEEE J Biomed Health Inform* 18(2):636–642
 - 21. Ban Z, Liu J, Cao L (2018) Superpixel segmentation using Gaussian mixture model. *IEEE Trans Image Process* 27(8):4105–4117
 - 22. Achanta R, Shaji A, Smith K, Lucchi A, Fua P, Süsstrunk S (2012) SLIC superpixels compared to state-of-the-art superpixel methods. *IEEE Trans Pattern Anal Mach Intell* 34(11):2274–2282
 - 23. Iakovidis DK, Chatzis D, Chrysanthopoulos P, Koulaouzidis A (2015) Blood detection in wireless capsule endoscope images based on salient superpixels. In: *2015 37th Annual International Conference of the IEEE Engineering in Medicine and Biology Society (EMBC)* (pp. 731–734). IEEE
 - 24. Xing X, Jia X, Meng MH (2018) Bleeding detection in wireless capsule endoscopy image video using superpixel-color histogram and a subspace KNN classifier. In: *2018 40th Annual International Conference of the IEEE Engineering in Medicine and Biology Society (EMBC)* (pp. 1–4). IEEE
 - 25. Yuan Y, Wang J, Li B, Meng MQH (2015) Saliency based ulcer detection for wireless capsule endoscopy diagnosis. *IEEE Trans Med Imaging* 34(10):2046–2057
 - 26. Maghsoudi OH (2017) Superpixel based segmentation and classification of polyps in wireless capsule endoscopy. In: *2017 IEEE Signal Processing in Medicine and Biology Symposium (SPMB)* (pp. 1–4). IEEE
 - 27. Ghosh T, Fattah SA, Shahnaz C, Kundu AK, Rizve MN (2015) Block based histogram feature extraction method for bleeding detection in wireless capsule endoscopy. In: *TENCON 2015–2015 IEEE Region 10 Conference* (pp. 1–4). IEEE
 - 28. Suman S, Malik AS, Pogorelov K, Riegler M, Ho SH, Hilmi I, Goh KL (2017) Detection and classification of bleeding region in WCE images using color feature. In: *Proceedings of the 15th International Workshop on Content-Based Multimedia Indexing* (p. 17). ACM
 - 29. Pogorelov K, Suman S, Hussin FA, Malik AS, Ostroukhova3 O, Riegler M, Halvorsen P, Ho SH, Goh KL (2019) Bleeding detection in wireless capsule endoscopy videos—color versus texture features. *Medical Imaging*
 - 30. Kundu AK, Fattah SA, Rizve MN (2018) An automatic bleeding frame and region detection scheme for wireless capsule endoscopy videos based on interplane intensity variation profile in normalized RGB color space. *J Healthc Eng* 2018.
 - 31. Deeba F, Mohammed SK, Bui FM, Wahid KA (2016) Unsupervised abnormality detection using saliency and retinex based color enhancement. In: *2016 38th Annual International Conference of the IEEE Engineering in Medicine and Biology Society (EMBC)* (pp. 3871–3874). IEEE
 - 32. Sainju S, Bui FM, Wahid KA (2014) Automated bleeding detection in capsule endoscopy videos using statistical features and region growing. *J Med Syst* 38(4):25
 - 33. Chaibou MS, Conze PH, Kalti K, Solaiman B, Mahjoub MA (2017) Adaptive strategy for superpixel-based region-growing image segmentation. *J Electron Imaging* 26(6):061605
 - 34. Rahim T, Usman MA, Shin SY (2019) A survey on contemporary computer-aided tumor, polyp, and ulcer detection methods in wireless capsule endoscopy imaging. *arXiv preprint arXiv:1910.00265*
 - 35. Faigel DO, Cave DR (2008) Capsule endoscopy, Saunders Elsivier
 - 36. Video Journal and Encyclopedia of GI Endoscopy, Elsevier Inc, [Online]. Available: <http://www.vjgi-endoscopy.com/toc> a-c. [Accessed Sept 2019]
 - 37. Stephen Cobeldick, <<https://www.mathworks.com/matlabcentral/fileexchange/48155>> Copyright (c) 2019, Accessed 10 Oct 2019

Publisher's note Springer Nature remains neutral with regard to jurisdictional claims in published maps and institutional affiliations.



S. Rathnamala Assistant Professor in the Department of Information Technology at Sethu Institute of Technology, Kariapatti, Virudhunagar District-626115, Tamilnadu. She completed her under graduation in Information Technology at R.V.S College of Engineering & Technology Dindigul Tamil Nadu in 2005. Later she finished her post-graduation in the same discipline in 2009 from Manonmaniam Sundaranar University, Tirunelveli, Tamil Nadu. Her research work was on Medical Image Processing.



S. Jenicka (Associate Professor, Sethu Institute of Technology, Pulloor, Kariapatti Taluk, Virudhunagar District) completed her under graduation in Computer Science and Engineering at Thiagarajar College of Engineering, Madurai, Tamil Nadu in 1994. Later she finished her post-graduation in the same discipline in 2009 from Manonmaniam Sundaranar University, Tirunelveli. She completed a doctorate in Computer Science and Engineering in 2014. Her research work was on ‘Texture based classification of remotely sensed images’. Her interests include Satellite image processing and texture segmentation.